ACS APPLIED MATERIALS & INTERFACES

Research Article

www.acsami.org

Effect of Nanostructure Building Formation on High Current Field Emission Properties in Individual Molybdenum Nanocones

Yan Shen, Ningsheng Xu, Shaozhi Deng,* Shuai Tang, Yu Zhang, Fei Liu, and Jun Chen

Guangdong Province Key Laboratory of Display Material and Technology, State Key Laboratory of Optoelectronic Materials and Technologies, and School of Physics and Engineering, Sun Yat-sen University, Guangzhou 510275, China

Supporting Information

ABSTRACT: The building formation of a one-dimensional nanostructure greatly affects its physical properties. By controlling the supersaturation of deposited molybdenum (Mo) vapor, two kinds of nanostructure building formations can be synthesized in Mo nanocones (spiral- and stacking-type) through a thermal evaporation process. The field emission performances of these two formations are vastly different, particularly with respect to their high current properties. The maximum current of a spiral-type individual Mo nanocone is five times that of the stacking-type nanocone. Electrical transport may not be the decisive factor for this difference because both types of individual Mo nanocones have similar excellent conductivities. Heat conduction during the high current emission process has been considered a primary factor, and it strongly depends on the number of internal nanostructure boundaries in the Mo nanocone. These results indicate that nanostructure building formations with fewer inner boundaries in Mo nanocones contribute to a higher current field emission performance when applied to vacuum electron devices.

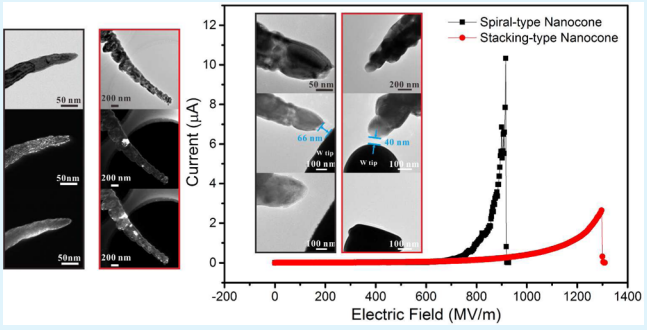

KEYWORDS: *molybdenum nanocone, structure building formation, electrical transport, heat conduction, high current field emission properties*

INTRODUCTION

One-dimensional metal nanostructures have garnered significant attention due to their unique geometric morphology and special crystal structure in numerous applications, such as optics,[1] electricity,[2,3] thermology,[4] magnetics,[5] and gas sensitivity.[6] However, the building formation of a nanostructure determines the facade and orientation of its structure and thus greatly affects its physical properties. Au nanostructures have been demonstrated to be shape-selective through UV-photoactivation, and the surface enhanced Raman scattering (SERS) intensity increases with the change in their shapes from nanospheres to -rods to -wires to -prisms.[7] Tungsten nanowires have been reported to show anisotropy in the resistivity size effect on the basis of their different longitudinal orientations along the ⟨100⟩, ⟨110⟩, and ⟨111⟩ crystallographic directions.[8] Hence, the controllable synthesis of nanostructure building formation is a challenging problem as well as understanding how these formations affect physical properties.

Molybdenum (Mo) is an important transition metal with a high melting point and high electrical conductivity.[9,10] In recent years, a large number of studies has focused on the preparation of one-dimensional molybdenum nanostructures and their potential applications.[2,11,12] We have been developing a polycrystalline molybdenum nanoscrew (a nanocone with a helical surface morphology) with high conductivity and excellent field emission properties.[13] In particular, Mo nanoscrew films shows high field emission current densities in both direct-current (DC) and pulsed driver modes and should have potential applications as cold cathode materials for high current vacuum electron devices. In this work, we present evidence for how the building formation of nanostructures in individual molybdenum nanocones affects high current field emission performance. Two kinds of molybdenum nanocones (spiral- and stacking-type) are prepared by controlling the supersaturation of depositing Mo vapor. The crystalline structures of these two types of nanocones are analyzed along with the differences in their field emission abilities. The corresponding mechanisms regulating these differential properties are discussed.

RESULTS AND DISCUSSION

Morphology and Structure. Figure 1a–d show top and side view SEM images of the spiral- and stacking-type molybdenum nanocones. These nanostructures are distributed all over the substrate surface. The insets are high-magnification SEM images of the individual nanostructures. Both types of nanostructures are tapered with a sharp tip and thick bottom. Noteworthy is the fact that the stacking-type Mo nanocones are

Received: December 17, 2014
Accepted: January 27, 2015
Published: January 27, 2015

DOI: 10.1021/am508914h
ACS Appl. Mater. Interfaces 2015, 7, 3825–3833

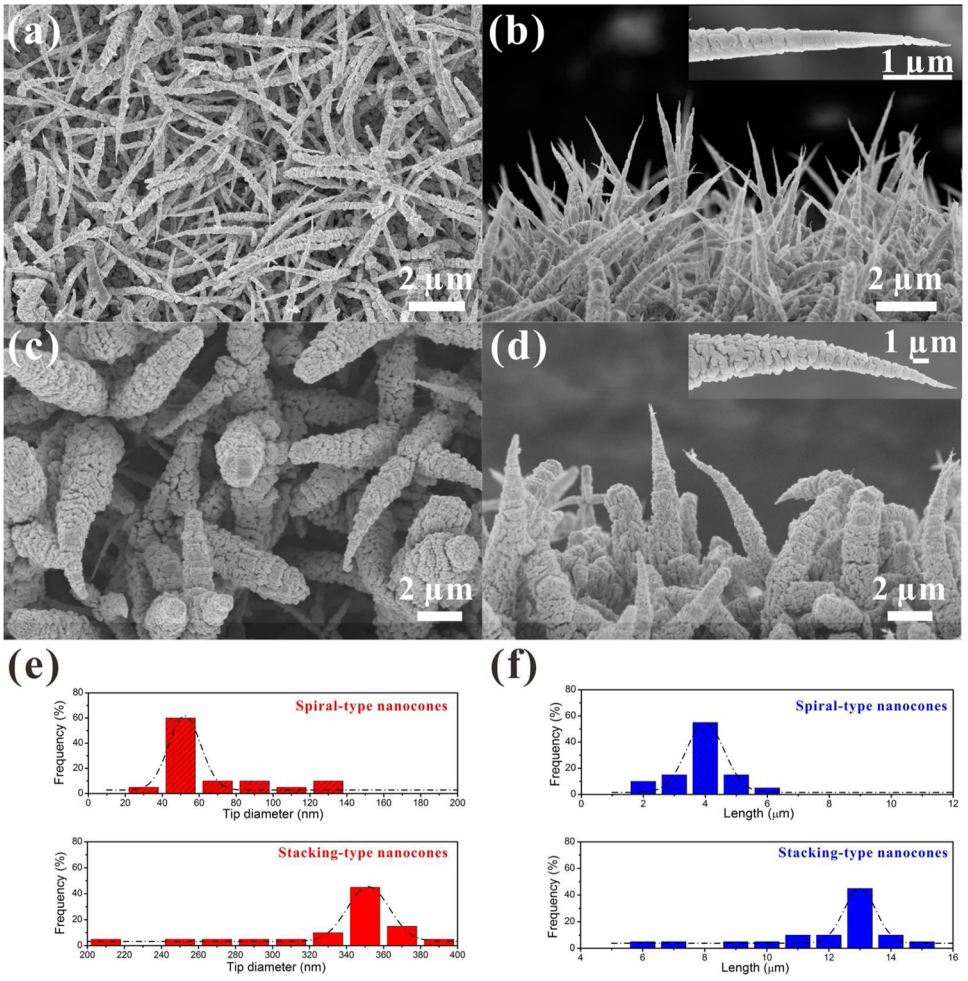

Figure 1. SEM images of spiral- and stacking-type molybdenum nanocone films. (a) Top- and (b) side-view SEM images of spiral-type Mo nanocones. (b, inset) High-magnification SEM image of an individual spiral-type nanocone. (c) Top- and (d) side-view SEM images of stacking-type nanocones. (d, inset) High-magnification SEM image of an individual spiral-type nanocone. (e) Tip diameter and (f) length distribution of both types of nanocones.

formed by a number of unordered grains, whereas the spiral-type are clearly more organized. The statistical distributions of the nanocone morphologies are presented in Figure 1e and f; the average tip diameter and length of the spiral-type Mo nanocones are 50 nm and 4 μm, respectively, whereas the stacking-type are thicker and longer with corresponding average values of 350 nm and 13 μm, respectively.

Transmission electron microscopy (TEM) has been employed to further study the detailed structure differences between the spiral- and stacking-type nanocones. Figure 2a shows a low-magnification TEM image of a single spiral-type nanocone. It reveals that the arrangement of molybdenum grains here is ordered and regular. A high-magnification TEM image of area B in Figure 2a is presented in Figure 2b. The corresponding high-resolution TEM (HRTEM) image (Figure 2c) verifies that the selected grain is crystalline with mean lattice spacing of 0.22 nm between two adjacent planes, which is consistent with the {110} planes of the body-centered cubic (bcc) molybdenum. Moreover, we selected area D in Figure 2a for electron diffraction analysis, and the tip of the sample almost presents as single crystal (Figure 2d). Each grain participating in the spiral growth must have a good bcc structure because the selected area electron diffraction (SAED) patterns are sharp and ordered. Dark-field TEM images (Figure 2e and f) obtained using different diffraction electron beams can also be used as evidence that the composing grains have

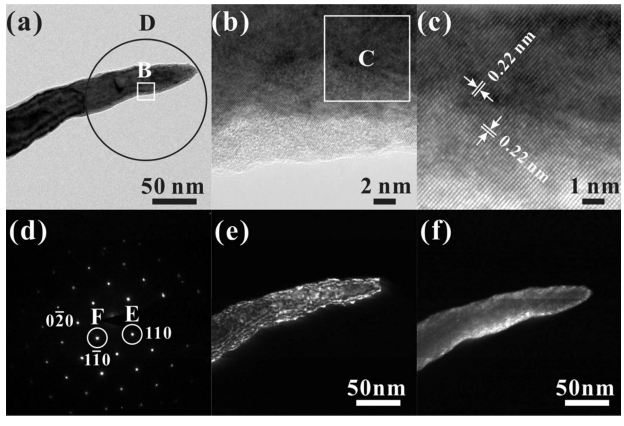

Figure 2. (a) Typical TEM image of an individual spiral-type Mo nanocone. (b) High-magnification TEM image of area B in (a). (c) HRTEM image of area C in (b). (d) Selected area electron diffraction (SAED) patterns of area D in (a). (e, f) Dark-field TEM images of the sample obtained using diffraction electron beams E and F in (d), respectively.

DOI: 10.1021/am508914h
ACS Appl. Mater. Interfaces 2015, 7, 3825−3833

almost the same orientation, and that the whole spiral-type nanocone has a relatively good single-crystalline nature.

Another structure type has also been observed. Figure 3a shows a typical TEM image of a stacking-type nanocone sample

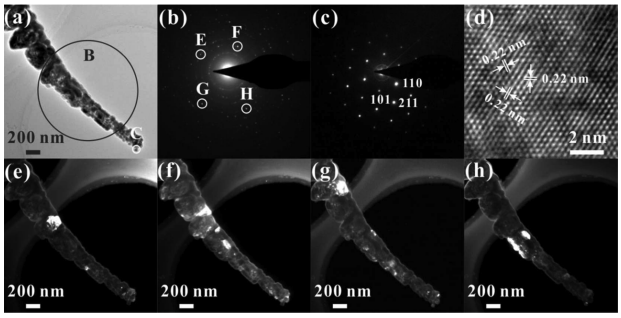

Figure 3. (a) Typical TEM image of an individual stacking-type Mo nanocone. (b) SAED patterns of area B in (a). (c) SAED patterns of area C in (a). (d) HRTEM image of area C in (a). (e–h) Dark-field TEM images of the sample obtained by diffraction electron beams (e) E, (f) F, (g) G, and (h) H in (b).

with a large number of stacking grains along its longitudinal growth direction, namely, a large number of interfaces. SAED of area B reveals Debye–Scherrer concentric rings of (110), (200), (211), and so on (Figure 3b), which indicates the existence of a polycrystalline structure in the sample. A grain on the top of the nanocone was chosen for SAED and HRTEM analysis (Figure 3c and d) and reveals that the stacking Mo grains likewise have a single crystalline bcc structure. In addition, the dark-field TEM images obtained by diffraction electron beams E, F, G, and H in Figure 3b reveal different grains and boundaries, confirming that these grains are not in the same plane and have various orientations (Figure 3e to h). TEM analysis reflects that the stacking-type nanocones tend to be polycrystalline with more defects, such as dislocations, boundaries, and stacking faults, than the spiral-type nanocones.

Field Emission Properties of Individual Nanocones. Figure 4 shows the high current field emission properties of various single Mo nanocones. Individual spiral- and stacking-type nanocones were selected to have DC field emission measurements at a vacuum gap of ~2 μm in situ in a modified SEM system. In the current versus electric field (I–E) characteristic curves (Figure 4a), the individual spiral-type nanocones are shown to generally get to a maximum emission current over 10 μA before breakdown of the vacuum; the stacking-type values, however, are much smaller at close to 5 times less than those of the spiral-type (Figure 4b). The SEM images in Figure 4c and d reveal the morphology of individual nanocones before and after vacuum breakdown, respectively. The sharp tip of the spiral-type nanocone could be fused (emphasized in the black circle) after a vacuum breakdown. However, the melted locations of the stacking-type nanocones were in the midcourse phase, and the entire emitter was irreversibly damaged. These results indicate that the spiral-type nanocone has a higher current field emission performance than the stacking-type.

Mechanism for the Differential Emmission Capacities. Here, we will discuss the reasons such a difference exists. It is known that the maximum emission current of an individual is limited by the temperature it can handle and can be determined

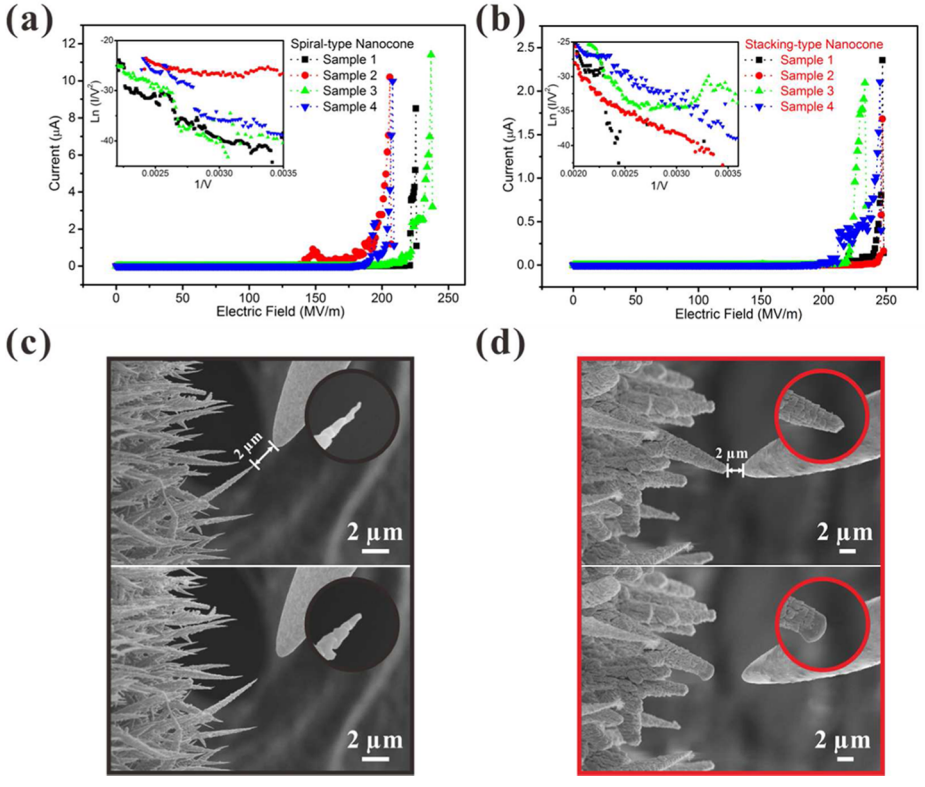

Figure 4. Field emission measurements of individual nanocones in situ in a modified SEM system. (a and b) Emission current versus electric field (I–E) characteristic curves of individual (a) spiral- and (b) stacking-type nanocones and their corresponding F–N plots at the high electrical field region (insets). (c and d) SEM images of a (c) spiral- and (d) stacking-type sample before (top) and after (bottom) vacuum breakdown.

DOI: 10.1021/am508914h
ACS Appl. Mater. Interfaces 2015, 7, 3825–3833

by its electrical transport and heat conduction capacities in the presence of an external electric field.[14]

For the individual stacking-type Mo nanocones, good Ohmic contacts exist between the samples and the substrate (Figure S1 in the Supporting Information). Moreover, their electrical conductivities (κ) were estimated to range from $(3.28-7.01) \times 10^4\ \Omega^{-1}\mathrm{cm}^{-1}$ (Figure S2, Equations S1−S4, and Table S1 in the Supporting Information), which is on the same order of magnitude as the spiral-type ($(3.44\sim7.74) \times 10^4\ \Omega^{-1}\mathrm{cm}^{-1}$).[13] This means that the differences in the building of the structures has no obvious influence on the electrical transport properties of the nanocones, at least at room temperature.

Attention was then focused on the heat conduction abilities of the nanocones. Under a high external electric field, the current flow in a nanocone varies with temperature due to heating at its apex, which causes elevation in the emission current. If the heat dissipation from the top end of the emitter to the substrate is not enough to sustain thermal equilibrium, a positive feedback process will result in an increasing temperature until it reaches its melting point and vacuum breakdown occurs. In other words, in our case, thermal conductivity (λ) is a variable that is related to the temperature and microcosmic crystal structure.

The thermal conductivity of the body is determined by inelastic collisions and scatter of the phonons or, as an analogy to kinetic theory, by the mean free path of the phonons. Debye has defined the λ of such a body as[15]

$$\lambda = \frac{1}{3}cvl \tag{1}$$

where c is the volume specific heat, v is the elastic wave velocity, and l is the mean free path of the phonons. In a real body, like polycrystalline Mo nanocones, a number of scattering mechanisms may limit the mean free path of phonons. Klemens has reported that if more than one mechanism is present the overall mean free path due to the multiple processes is given by[16]

$$\frac{1}{l_u} = \frac{1}{l_1} + \frac{1}{l_2} + \dots \tag{2}$$

where l_u is the overall mean free path and l_1, l_2, and so forth are the mean free paths of individual processes that are independent of each other. Imperfections and inhomogeneities in a body, which include defects, impurities, boundaries, and pores, also act as scattering centers of phonons and thus further reduce their mean free path. Hence, the total thermal resistivity (inverse of conductivity) of a polycrystalline body can be described by the function

$$\frac{1}{\lambda} = \frac{1}{\lambda_1} + \frac{1}{\lambda_2} + \frac{1}{\lambda_3} + \dots \tag{3}$$

From eq 3, $1/\lambda_1$ is expressed as the thermal resistivity generated by the scattering of the phonons inside grains, which is be given by[17]

$$\frac{1}{\lambda_1} = \frac{AT^m}{e^{\theta_D/2T}-1} \tag{4}$$

where θ_D is the Debye temperature, A is a constant, and m is a value between 1 and 2. In the process of large current field emissions, the temperature (T) is far higher than θ_D, and eq 4 can thus be simplified to

$$\frac{1}{\lambda_1} = AT^{m+1} \tag{5}$$

Next, $1/\lambda_2$ is expressed as thermal resistivity due to the nonuniformity of impurities, which is given by

$$\frac{1}{\lambda_2} = BNT^n,\ 0 < n < 1 \tag{6}$$

where N is the number of impurity atoms per unit length and B is a constant. Because no second phase appears in pure Mo nanocones, the effectiveness of impurities to reduce thermal conductivity can be ignored. Next, $1/\lambda_3$ is the thermal resistivity affected by the scattering of phonons at grain boundaries and pores, which can be expressed as

$$\frac{1}{\lambda_3} = \frac{1}{VLT^3} \tag{7}$$

where L is the grain size. It has been known that the contribution of boundary and pore scattering to phonons for total resistivity is dominant at temperatures near absolute zero,[18] whereas it should be negligible for polycrystals above room temperature. However, the volume effect of crystal boundaries and pores with their own thermal conductivity may be considerable; thus, the relation can be developed such that[19]

$$\frac{1}{\lambda_4} = \frac{1}{\lambda_c}(1 + Cu) \tag{8}$$

where $1/\lambda_c$ is the thermal resistivity of a single crystal, u is the number of boundaries per unit length, and C is a positive constant. Lastly, it is also necessary to consider imperfections on small scale defects (e.g., atom vacancies and dislocations) separate from the large-size boundaries and pores discussed above. The effectiveness of this process can be described above the Debye temperature by the function[19]

$$\frac{1}{\lambda_5} = aT + b \tag{9}$$

where a is determined by the lattice conductivity and b depends on the concentration and type of imperfections.

Consequently, the total thermal resistivity before vacuum breakdown for polycrystalline Mo nanocones under a high current field emission can be expressed as

$$\frac{1}{\lambda} = AT^{m+1} + \frac{1}{\lambda_c}(1 + Cu) + aT + b \tag{10}$$

Unfortunately, it is very difficult to fit eq 10 because of the absence of relevant experimental measurements (e.g., temperature). Here, we assume that the scattering of phonons in the interior of grains and small-size defects are similar in the different types of individual Mo nanocones. Thus, the large-scale boundary effectiveness can be the decisive factor for the thermal carrying capability as well as the high current emission performance. From eq 8, it can be inferred that the fewer boundaries per unit length that there are in an emitter, the smaller the thermal resistivity and the greater the emission current will be. As described in Figures 1−3, the number of composing grains in the stacking-type nanocones is higher than in the spiral-type, and the stacking-type has a larger cross sectional area. Therefore, the number of boundaries per unit length (u) in the former should be much higher than in the latter, which may explain why the stacking-type nanocones always sustain a poorer emission current than the spiral-type.

DOI: 10.1021/am508914h
ACS Appl. Mater. Interfaces 2015, 7, 3825−3833

In situ field emission measurements of individuals in a modified TEM system have been employed to prove such view in a microcosmic way. Figure 5 gives the emission current

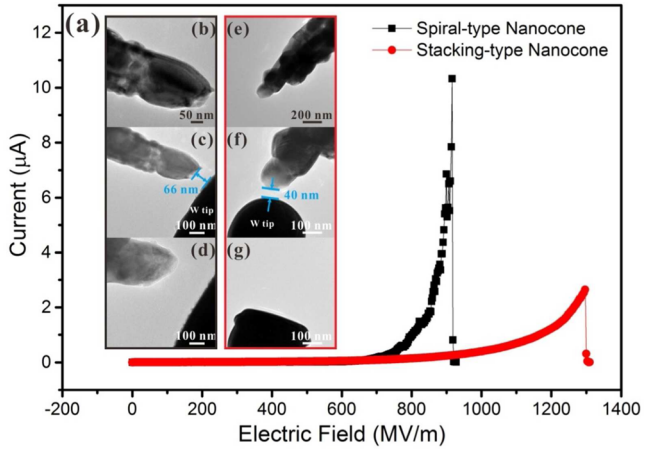

Figure 5. Field emission measurements of individual nanocones in situ in a modified TEM system. (a) Emission current versus electric field (I–E) characteristic curves of individual spiral- and stacking-type nanocones. (b–d) TEM images of a spiral-type sample before and after vacuum breakdown, respectively. (e–g) TEM images of a stacking-type individual before and after vacuum breakdown, respectively.

versus electric field (I–E) characteristic curves of individual spiral- and stacking-type nanocones and their corresponding TEM images before and after vacuum breakdown. Similar to the results presented in Figure 4, a single spiral-type sample can obtain an emission current as high as 10 μA, whereas the stacking-type can get to only ~2 μA. Both types of emitters have resulted in differing degrees of damage when vacuum breakdown occurs. The stacking-type sample was even completely removed along with fusion of the tungsten microprobe anode.

To observe boundary transformation during the field emission process and its effects on high emission current properties, we chose a spiral-type individual with clear constructing grain formation and boundaries as seen in Figure 6a. Figure 6b shows a high-magnification TEM image of area B in Figure 6a. Four representative areas have been selected for the further HRTEM and fast Fourier transform (FFT) analysis. Among them, regions 1 and 3 represented different stacking grains, whereas regions 2 and 4 corresponded to different locations on the grain boundary. From the HRTEM images in Figure 6c, the stacking grains were indeed found to be bcc structural molybdenum with mean lattice spacing of 0.22 nm between two primary adjacent planes. The FFT images of regions 2 and 4 reveal two sets of spots, indicating that the position of the stacking boundary is seen.

Next, an external electric field was applied until the emission current from the nanocone was as high as 1 μA. The corresponding current versus electric field (I–E) characteristic curves are given in Figure 7a. Some visual variation could be observed in this process (Figure 6e). As seen in Figure 6f, a small deflection (~10 degrees) occurred on the grain presented in region 1. The region 3 corresponding grain also had an obvious orientation change. Otherwise, regions 2 and 4 show the same crystal orientation as region 1, indicating that the original boundary position has been occupied by the stacking grain. Considering the fact that boundaries have less heat conducting ability than interior grains, they are more likely to accumulate heat during field emission process. The generated heat resulted in deformation and deflection of these grains, and ultimately caused a position change of the boundary due to extrusion of the grains against one another.

When the emission current was increased to 2 μA (Figure 7b), significant changes in the overall appearance of this area were observed. In Figure 6h, the original boundary became very fuzzy, and the surrounding grains tended to recrystallize. The HRTEM and FFT analyses of regions 1–4 (Figure 6i) also revealed that the crystal structure of various locations were moving toward a fairly consistent orientation, which differed greatly from the orientations without an externally applied field. When the current of the nanocone emitter was increased to ~10 μA (Figure 7c), thorough vacuum breakdown damage occurred. At this stage, the marked area recrystallized into a whole grain, and the original grain boundary disappeared completely (Figure 6k). It is worth noting that due to the excessive current running throughout the emitter, the metallic bcc structure molybdenum gradually became amorphous, which is reflected in the FFT images of regions 1–4 (Figure 6l).

The selected spiral-type nanocone can sustain a very high emission current, whereas internal stacking grains and their boundaries lack the ability to transmit much heat. In fact, a material that is completely single crystalline has perfect thermal conductivity without any weakening. A number of single crystals and polycrystals were measured, and the thermal conductivity of the single crystal was invariably higher than that of the polycrystalline material.[20] Given this observation, a structural building with as few interfaces as possible may be a good method for gaining higher current field emission properties for the Mo nanocone.

Field Emission Properties of the Films. Field emission properties of the spiral- and stacking-type Mo nanocone films with an area of 0.02 cm^2 were investigated in an ultra-high vacuum system (~7.5×10^{-9} Torr). The samples were studied using a diode measurement technique at a vacuum gap of 200 μm under DC and pulsed voltage driver modes. After a few cycles of applying an electric field in the gap, the field emission reached a stable and repeatable stage, and the current versus electric field (I–E) curves of both nanocone types were recorded (Figure 8a). The turn on field (E_{to}) is defined as the applied electric field needed to induce a field emission current density of 10 $\mu A\ cm^{-2}$ and is in the range of 1.5–2 MV m^{-1} for the spiral-type samples, whereas the value for the stacking-type nanocone films is much higher at ~3.8 MV m^{-1}. From the perspective of the field enhancement factor (β), an emitter with a longer length and thinner diameter easily has a larger aspect ratio ($2L/d$) and lower turn on field (E_{to}). In this study, the calculated aspect ratio values of the spiral- and stacking-type nanocones are 160 and 74.3, respectively. This may explain why spiral-type nanocones generally have a lower turn on field. Additionally, the largest obtained current densities of spiral-type nanocones are >100 mA cm^{-2}, whereas the stacking-type can reach only ~32.73 mA cm^{-2}. Moreover, the corresponding F–N plots of both types exhibit almost linear dependence, revealing that their emission behaviors are consistent with FN theory.

Figure 8b shows the field emission stability curves of the nanocone films. The spiral-type nanocones are shown to have a very stable field emission even though the current density is as high as 50 mA cm^{-2}. Thermionic emission will gradually

DOI: 10.1021/am508914h
ACS Appl. Mater. Interfaces 2015, 7, 3825–3833

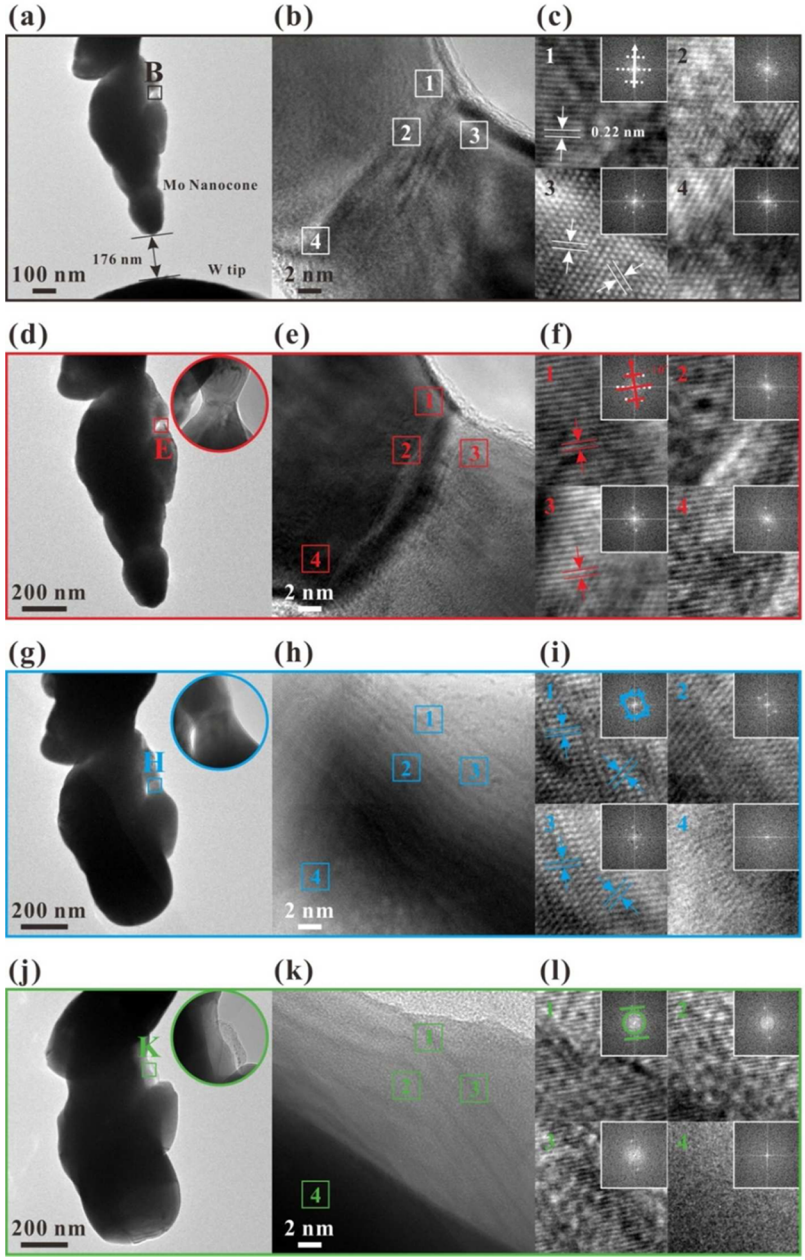

Figure 6. In situ TEM analysis of a spiral-type nanocone with constructing grain formation and their boundaries (a–c) before field emission measurements and after with an emission current as high as (d–f) 1 μA, (g–i) 2 μA, and (j–l) 10 μA.

increase its effect in the applied high electric field only when the current density is >70 mA cm^{-2}. However, the emission of the stacking-type samples less stable. When the current density is just over 25 mA cm^{-2}, thermionic emission increases suddenly with an amplification of 28%.

Figure 8c gives the input voltage waveform and the corresponding output current waveforms of the nanocone films under the pulsed voltage driver mode. These waveforms were recorded by an oscilloscope at a pulse width of 5 μs and frequency of 2 kHz. The input waveform marks the supplied high voltage of the pulse power, whereas the output waveform stands for the calculated current through the external sample resistance (20Ω). The obtained maximum emission current of the spiral-type nanocone films is ~12.1 mA at an anode voltage of 7.4 kV, and its corresponding current density can get as high as 605 mA cm^{-2}. However, the stacking-type nanoscrews recorded only 4.12 mA and 206 mA cm^{-2} the maximum emission current and corresponding current density, respectively. Such differences also can be distinguished through the I–E curves of the nanocone types (Figure 8d). These measurements indicate that the spiral-type Mo nanocone film has an excellent and stable field emission performance that is dramatically better than that of the stacking-type.

CONCLUSION

In summary, molybdenum nanocones present with different structural building formations by controlling the supersaturation (σ) of Mo vapor. Spiral- and stacking-type Mo nanocones have been compared with respect to their morphology, detailed structure, and high current field emission properties. The stacking-type nanocones have longer thicker bodies than those of the spiral-type. However, the internal structure of the

DOI: 10.1021/am508914h
ACS Appl. Mater. Interfaces 2015, 7, 3825–3833

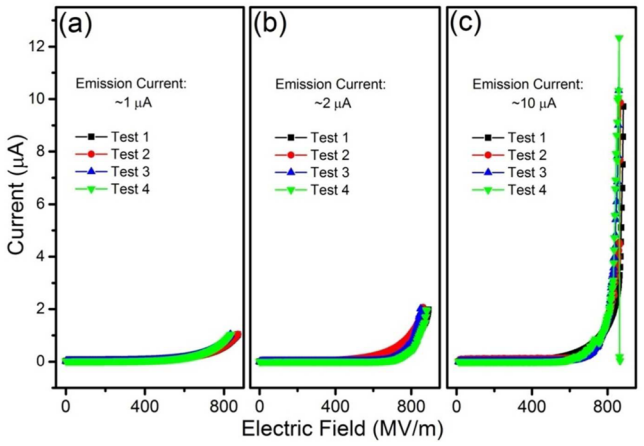

Figure 7. Field emission current versus electric field (I–E) characteristic curves corresponding to the spiral-type nanocone samples in Figure 6 with the emission current set as high as (a) 1 μA, (b) 2 μA, and (c) 10 μA.

stacking-type nanocones is more complicated with lots of boundaries and defects. The high current field emission performances are vastly different. The maximum emission current of an individual spiral-type nanocone is >10 μA, whereas the stacking-type can get only to ~2 μA. The mechanism for this difference has been discussed. Because both types have been confirmed to show remarkable electrical conductivities, heat transfer under a high electric field may be the key factor. Constructing grain formations with more boundaries per unit length cannot sustain overheating or too high of a current. In situ field emission measurements in a modified TEM system have been used to demonstrate such a view. Similar properties can be obtained from the field emission measurements of the nanocone films. The results indicate that a structure building formation with fewer inner interfaces in individual Mo nanocones should be an effective way to obtain high current field emission performance for potential electron device applications.

EXPERIMENTAL DETAILS

Growth Process of Spiral- and Stacking-Type Molybdenum Nanocones. Basic chemical reactions and growth processes to obtain metallic Mo nanostuctures have been described in our previous reports.[13,21] Circular stainless steel as the substrate and a Mo boat as the evaporation source were washed with acetone and alcohol, consecutively, in an ultrasonic bath. The boat and substrates were then placed in the center of a vacuum chamber at a certain distance from each other. When the chamber was evacuated to ~5×10^{-2} Torr, the boat temperature was gradially increased to exceed 1623 K. For the spiral-type nanocones, the temperature of the Mo boat (T_v) and the distance between boat and substrates (d) were 1623 K and 3 mm, respectively. Next, for the stacking-type products, T_v was raised to 1723 K, and d expanded to 5 mm. High-purity argon gas (99.99%; 80 standard cubic centimeters per minute (sccm)) and high-purity hydrogen gas (99.99%; 80 sccm) were introduced to the system throughout the entire process. After deposition for more than 15 min, formation of the different types of Mo nanocones was complete.

Growth Mechanism. The key structural difference depends on the supersaturation (σ) of Mo vapor, which is deeply influenced by the temperature of the Mo boat (T_v) and the distance between boat and substrates (d). Figure 9a gives a schematic diagram of the evaporation

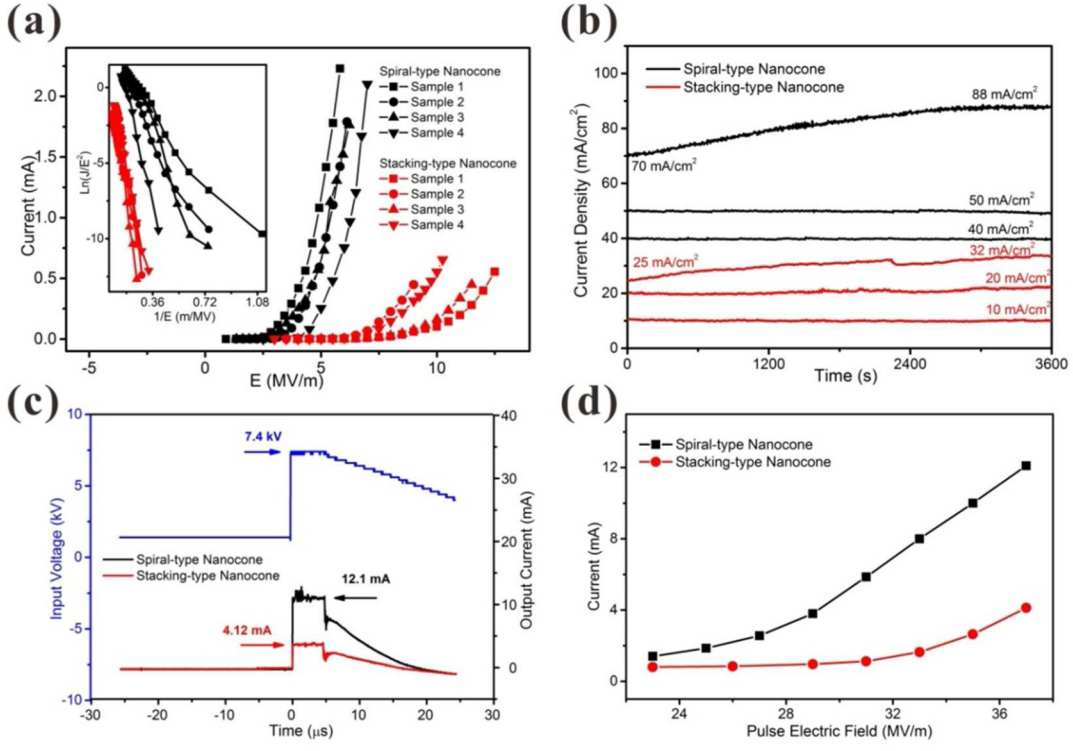

Figure 8. Field emission properties of both types of Mo nanocone films. (a) Field emission current versus electric field (I–E) curves of the spiral- and stacking-type Mo nanocone films under the DC voltage driver mode. The inset is their corresponding F–N plots. (b) Emission stability curves of the different sample types. (c) The input voltage waveform and the output current waveforms of the different films types under the pulsed voltage driver mode. The left side marks the supplied high voltage of pulse power, whereas the right side is the obtained emission current. (d) I–E curves of the samples at a vacuum gap of 200 μm and a frequency of 2 kHz.

DOI: 10.1021/am508914h
ACS Appl. Mater. Interfaces 2015, 7, 3825–3833

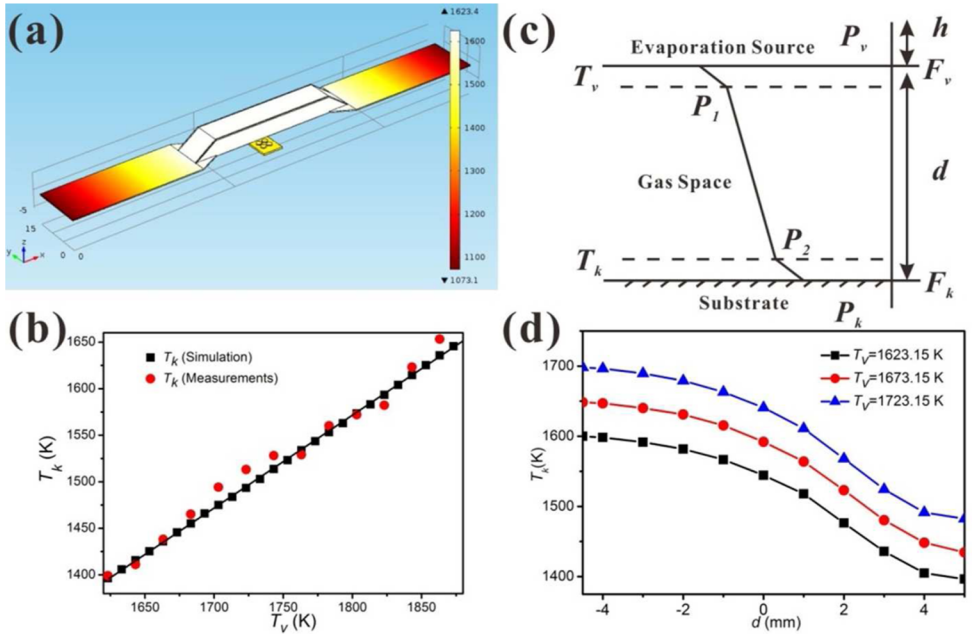

Figure 9. Growth condition simulation of spiral- and stacking-type nanocones (simulated by Comsol Multiphysics 4.3a). (a) The temperature conduction and radiation distribution diagram at a Mo boat temperature (T_v) of 1623 K and distance (d) of 5 mm. (b) Curve of the substrate versus Mo boat temperature (T_k–T_v) with d = 5 mm. (c) Schematic diagram of the material evaporation–condensation process. (d) Substrate temperature versus distance (T_k–d) curves simulated at different values of T_v.

source and substrates. Ignoring the nonuniformity of resistive heating, the center temperature of the Mo boat can be taken as the source temperature (T_v). Using the software Comsol Multiphysics 4.3a, we simulated the temperature distribution of the upper surface of the substrates, which was treated as the growth temperature of the Mo nanocones (T_k). As seen in Figure 9a, for instance, when T_v is 1623 K and d is 5 mm, the growth temperature T_k is simulated as 1396 K. Figure 9b reveals the growth temperature versus the temperature of the Mo boat (T_k–T_v) curve at d = 5 mm. We measured the actual temperature of substrates using an infrared thermometer and found that the experimental data is close to that of our simulation. The scheme diagram of the material evaporation–condensation process is shown in Figure 9c. In this diagram, P_v is the vapor pressure of Mo vapor at the evaporating surface F_v. It decreases to P_1 after moving through the gas diffusion layer on the evaporation surface, and then reduces to P_2 after moving through the gas space in the reaction chamber. It finally becomes P_k after moving through the gas diffusion layer of the condensation surface F_k. When the evaporation and condensation achieve a dynamic balance, we can build an expression regarding evaporation capacity per unit time per unit area[22]

$$N_v = N_k = \frac{P}{\sqrt{2\pi mkT}} \tag{11}$$

where N_v and N_k represent the number of evaporating and condensing Mo atoms per unit time per unit area, respectively, m is the quality of one Mo atom, k is the Boltzmann constant, and T is the temperature. In this process, some of the vapor Mo atoms have an elastic reflection on the phase interface and cannot be condensed. According to the principle of dynamic balance, the number of evaporating atoms should also be reduced. Therefore, the evaporation rate should be multiplied by a coefficient of condensation and expressed by the quality of evaporation per unit time per unit area (g cm^{-2} s^{-1})

$$W_m = 4.376 \times 10^{-4} \alpha P \sqrt{\frac{M}{T}} \tag{12}$$

By substituting the state equation of ideal gas (P=nkT), the equation can be written as

$$W_m = 4.376 \times 10^{-4} \alpha nk \sqrt{MT} \tag{13}$$

where α is the supersaturation of Mo atoms around evaporation surface, n is the corresponding density of gas atoms, and M is the molecular weight of molybdenum. At higher T_v, α and n will be larger. Furthermore, a shorter distance (d) also leads to a higher T_k, both of which help to improve the total supersaturation (σ) of depositing Mo atoms.

As shown in Figure 9d, the growth temperatures (T_k) to form spiral- and stacking-type Mo nanocones are simulated as 1435.9 and 1482.4 K, respectively. It is already known that at rather low values of σ, the growth of Mo nanocones tends to favor the spiral mode.[13] However, if σ is very high, excessive Mo atoms may condense and pile up. Considering the inadequate growth time and uneven energy, Mo crystals are very difficult to grow adequately in the form of perfect layered nucleation. As a result, the stacking-type nanocone has a different structure building style than the spiral-type.

Characterization. Scanning electron microscopy (Zeiss Supra55) was applied to investigate the morphology of grown nanocones. Transmission electron microscopy (FEI Tecnai G^2 F30) was employed to study the crystalline structures. The field emission measurements and electrical transport of the individuals were carried out in situ using a micropoint anode in both modified SEM (10 kV and 4 × 10^{-6} Torr) and TEM (300 kV) systems, the details of which were described in our previous reports.[13,21,23,24] In addition, the DC and pulsed field emission performance of spiral- and stacking-type nanocone films were compared using an ultra-high vacuum analysis system (7.5 × 10^{-9} Torr).

■ ASSOCIATED CONTENT

Supporting Information

Electrical transport properties and the corresponding conductivity calculations of the individual stacking-type molybdenum nanocones. This material is available free of charge via the Internet at http://pubs.acs.org.

■ AUTHOR INFORMATION

Corresponding Author

*E-mail: stsdsz@mail.sysu.edu.cn.

DOI: 10.1021/am508914h
ACS Appl. Mater. Interfaces 2015, 7, 3825–3833

Notes

The authors declare no competing financial interest.

■ ACKNOWLEDGMENTS

This work was supported by the National Key Basic Research Program of China (Grants 2013CB933601 and 2010CB327703), the National Natural Science Foundation of China (Grants U1134006 and 51290271), the Science and Technology Department of Guangdong Province, and the Fundamental Research Funds for the Central Universities.

■ ABBREVIATIONS

SEM, scanning electron microscopy
TEM, transmission electron microscopy
SAED, selected area electron diffraction
FFT, fast Fourier transform
DC, direct current

■ REFERENCES

(1) Pyayt, A. L.; Wiley, B.; Xia, Y. N.; Chen, A. T.; Dalton, L. Integration of Photonic and Silver Nanowire Plasmonic Waveguides. *Nat. Nanotechnol.* **2008**, *3*, 660−665.
(2) Zhou, J.; Deng, S. Z.; Gong, L.; Ding, Y.; Chen, J.; Huang, J. X.; Chen, J.; Xu, N. S.; Wang, Z. L. Growth of Large-Area Aligned Molybdenum Nanowires by High Temperature Chemical Vapor Deposition: Synthesis, Growth Mechanism, and Device Application. *J. Phys. Chem. B* **2006**, *110*, 10296−10302.
(3) Wang, S. L.; He, Y. H.; Fang, X. S.; Zou, J.; Wang, Y.; Huang, H.; Costa, P. M. F. J.; Song, M.; Huang, B. Y.; Liu, C. T.; Llaw, P. K.; Bando, Y.; Golberg, D. Structure and Field-Emission Properties of Sub-Micrometer-Sized Tungsten-Whisker Arrays Fabricated by Vapor Deposition. *Adv. Mater.* **2009**, *21*, 2387−2392.
(4) Diao, J. K.; Gall, K.; Dunn, M. L. Surface-Stress-Induced Phase Transformation in Metal Nanowires. *Nat. Mater.* **2003**, *2*, 656−660.
(5) Watson, S. M. D.; Mohamed, H. D. A.; Horrocks, B. R.; Houlton, A. Electrically Conductive Magnetic Nanowires Using an Electrochemical DNA-Templating Route. *Nanoscale* **2013**, *5*, 5349−5359.
(6) Walter, E. C.; Penner, R. M.; Liu, H.; Ng, K. H.; Zach, M. P.; Favier, F. Sensors from Electrode Posited Metal Nanowires. *Surf. Interface Anal.* **2002**, *34*, 409−412.
(7) Kundu, S. A New Route for the Formation of Au Nanowires and Application of Shape-Selective Au Nanoparticles in SERS Studies. *J. Mater. Chem. C* **2013**, *1*, 831−842.
(8) Choi, D.; Moneck, M.; Liu, X.; Oh, S. J.; Kagan, C. R.; Coffey, K. R.; Barmak, K. Crystallographic Anisotropy of the Resistivity Size Effect in Single Crystal Tungsten Nanowires. *Sci. Rep.* **2013**, *3*, 2591.
(9) Worthing, A. G. The Temperature Scale and the Melting Point of Molybdenum. *Phys. Rev.* **1925**, *25*, 846−858.
(10) Worthing, A. G. Physical Properties of Well Seasoned Molybdenum and Tantalum as a Function of Temperature. *Phys. Rev.* **1926**, *28*, 190−201.
(11) Zhou, J.; Xu, N. S.; Deng, S. Z.; Chen, J.; She, J. C.; Wang, Z. L. Large-Area Nanowire Arrays of Molybdenum and Molybdenum Oxides: Synthesis and Field Emission Properties. *Adv. Mater.* **2003**, *15*, 1835−1840.
(12) Milenkovic, S.; Smith, A. J.; Hassel, A. W. Single Crystalline Molybdenum Nanowires, Nanowire Arrays and Nanopore Arrays in Nickel-Aluminium. *J. Nanosci. Nanotechnol.* **2008**, *8*, 1−7.
(13) Shen, Y.; Xu, N. S.; Deng, S. Z.; Zhang, Y.; Liu, F.; Chen, J. A Mo Nanoscrew Formed by Crystalline Mo Grains with High Conductivity and Excellent Field Emission Properties. *Nanoscale* **2014**, *6*, 4659−4668.
(14) She, J. C.; Xu, N. S.; Deng, S. Z.; Chen, J.; Bishop, H.; Huq, S. E.; Wang, L.; Zhong, D. Y.; Wang, E. G. Vacuum Breakdown of Carbon-Nanotube Field Emitters on a Silicon Tip. *Appl. Phys. Lett.* **2003**, *83*, 2671−2673.
(15) Debye, P. Vortrage uber die Kinetische Theorie der Materie und Elektrizitat (Papers on the Kinetic Theory of Matter and Electricity); Wolfskehlvortrage, G., Teubner, B. G., Eds.; Leipzig and Berlin: Germany, 1914.
(16) Klemens, P. G. Thermal Conductivity of Dielectric Solids at Low Temperatures. *Proc. R. Soc. London, Ser. A* **1951**, *208*, 108−133.
(17) Cheng, K. J. *Solid State Physics*; People's Education Press: Beijing, China, 1959.
(18) Berman, R. Thermal Conductivity of Dielectric Solids at Low Temperatures. *Adv. Phys.* **1953**, *2*, 103−140.
(19) Charvat, F. R.; Kingery, W. D. Thermal Conductivity: XIII, Effect of Microstructure on Conductivity of Single-Phase Ceramics. *J. Am. Ceram. Soc.* **1957**, *40*, 306−315.
(20) Koenig, J. H.; Snyder, N. H. Ceramics. *Ind. Eng. Chem.* **1951**, *43*, 2208−2217.
(21) Shen, Y.; Deng, S. Z.; Zhang, Y.; Liu, F.; Chen, J.; Xu, N. S. Highly Conductive Vertically Aligned Molybdenum Nanowalls and Their Field Emission Property. *Nanoscale Res. Lett.* **2012**, *7*, 463−1−12.
(22) Gao, B. H.; Cui, S. Y. *Vacuum Physics*; Science Press: Beijing, China, 1983; p 587.
(23) She, J. C.; Xiao, Z. M.; Yang, Y. H.; Deng, S. Z.; Chen, J.; Yang, G. W.; Xu, N. S. Correlation Between Resistance and Field Emission Performance of Individual ZnO One-Dimensional Nanostructures. *ACS Nano* **2008**, *2*, 2015−2022.
(24) Zhang, Y.; Tang, S.; Deng, S. Z.; Chen, J.; Xu, N. S. Field Emission Characteristics of Vertical Few-Layer Graphene Using in Situ TEM. MRS Spring Meeting & Exhibit, San Francisco, CA, April 21−25, 2014.

DOI: 10.1021/am508914h
ACS Appl. Mater. Interfaces 2015, 7, 3825−3833